Supplementary Information for: Nitrogen Vacancies in Graphitic Carbon Nitride and their Role in Heterogeneous Photocatalysis

Alessandro Landi,*,† Francesco Ambrosio,*,‡ Nadia Bianchi,† Michele Loriso,‡ Lorenzo Malavasi,¶ Antonella Profumo,§ Julia Wiktor,‖ and Andrea Peluso†

†*Dipartimento di Chimica e Biologia Adolfo Zambelli, Università di Salerno, Via Giovanni Paolo II, I-84084 Fisciano (SA), Italy*

‡*Dipartimento di Scienze, Università degli Studi della Basilicata, Viale dell'Ateneo Lucano, 10 - 85100 Potenza, Italy*

¶*Energy and Materials Chemistry Group, Department of Chemistry and INSTM, University of Pavia,Via Taramelli 16, Pavia, 27100, Italy*

§*Department of Chemistry, University of Pavia,Via Taramelli 16, Pavia, 27100, Italy*

‖*Department of Physics, Chalmers University of Technology, SE-412 96 Gothenburg, Sweden*

E-mail: alelandi1@unisa.it; francesco.ambrosio@unibas.it

S1 Computational details

All density functional theory (DFT) calculations presented in this article are performed with the freely available CP2K-QUICKSTEP suite of codes[1–3] and are carried out on large supercell (cf. Table S1) constructed from the unit cell of g-C_3N_4 reported in Figure S1.

We employ Goedecker-Teter-Hutter pseudopotentials[4] for core electrons, with a cut-off of 600 Ry set for the plane waves and the MOLOPT double-zeta polarized basis set[2] used for valence electrons. Hybrid functionals calculations are carried out at an affordable computational cost and time, even for the largest systems considered here (up to 1008 atoms, cf. Table S1), by employing the auxiliary matrix method, conceived by CP2K-QUICKSTEP developers,[5–7] allowing for fast evaluation of exchange integrals on an auxiliary basis set. In particular, we use cFIT set[7], which was found to provide a good compromise between accuracy and affordable computational time (e.g. Ref. 8). Calculations involving unpaired electrons are performed adopting the unrestricted Kohn-Sham formalism and, in some cases, specifying the desired system multiplicity (*vide infra*).

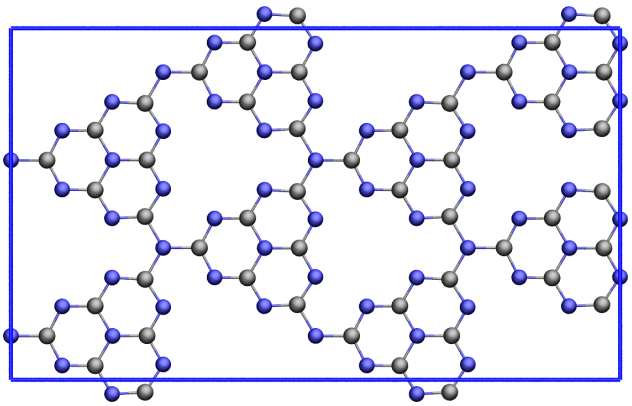

Figure S1: Idealized 2x2x1 flat $P6/m2$ heptazine-based network (see Figure 1 in main text) used as repetitive unit for the fully condensed system. The cell axes are: a=24.5380 Å and b=14.1660 Å.

Our choice of the density functional is guided by the need to alleviate the self-interaction error, typical of standard DFT methods, which would cause an incorrect description of charge localization in semiconductors.[9,10] To this end, we employ the functional already

Table S1: Number of atoms (N) and lattice parameters a, b, c for the supercells studied in this work

Cell	N	a	b	c
2×2	112	24.538	14.166	40.0
4×4	448	49.076	28.332	40.0
6×6	1008	73.614	42.498	40.0

used in Ref. 11, belonging to the PBE0 family of global hybrid functionals. In particular, it was shown in Ref. 11 that a fraction of Fock exchange equal to 18% fairly reproduce the electronic properties of g-C_3N_4. Non-local electron correlation is included in the functional via the scheme developed by Vydrov and Van Voorhis,[12,13] preserving the original value of 6.3 for the parameter b, which regulates the extent of dispersion interactions. The particular

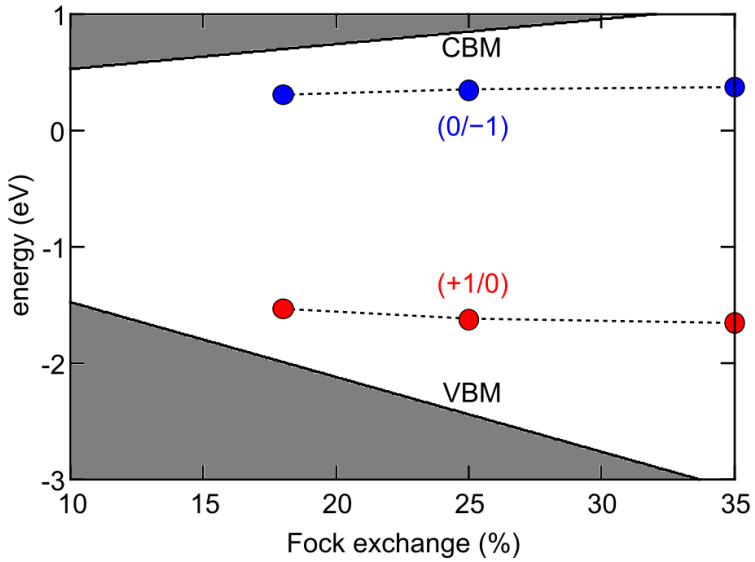

Figure S2: Valence band maximum (VBM) and conduction band minimum (CBM) of g-C_3N_4, along with adiabatic charge transition levels of V_N(C) in the constrained planar geometry, as a function of the fraction of Fock exchange α included in the hybrid functional. All values are given in eV and are referred to the valence band maximum for each system.

nature of two-dimensional materials, whose reduced dimensionality cause the band edges to experience a reduced screening while the localized defects are subject to bulk-like screening,[14] demands further inspection of the associated defect levels. For this reason, we here further show that, for the vacancies considered in this work, the position of charge transition levels

is robust against the fraction of Fock exchange α included in the functional, in line with what has been observed for solid and liquid condensed-phase systems.

This is proven in Figure S2, where we show, as a meaningful example, the valence and conduction band edges of g-C_3N_4, along with the adiabatic charge transition of the central nitrogen vacancy (cf. main text), as a function of the fraction of Fock exchange α incorporated in the global hybrid functional. The position of the defect levels are found to be fairly constant vs. α, when aligned with respect to a physical reference (in this case, the average electrostatic potential), as previously observed for three-dimensional materials and liquids.[15–17]

In all geometry optimizations, the in-plane lattice parameters (a, b) were kept fixed at the values optimized for the pristine g-C_3N_4 unit cell, scaled by the appropriate supercell dimensions (n = 2, 4, 6). The out-of-plane lattice parameter c (vacuum gap) was also kept fixed and equal to 40 Å.

S2 Charge transition levels calculations

The energy level associated with the adiabatic transition of a defect from the charge state q to q', $\mu[X(R_q, q)/X(R_{q'}, q')]$, is formally defined as the value of the electron chemical potential at which the formation free energy of the defect in the two charge states is equal, i.e. $E_\mathrm{f}[X^q(R_q)] = E_\mathrm{f}[X^{q'}(R_{q'})]$,[18,19] and can be evaluated from quantities computed from DFT calculations:[8,20]

$$\mu^\mathrm{ad}(X^q/X^{q'}) = \frac{E[X^q(R_q)] - E[X^{q'}(R_{q'})]}{q' - q} + \frac{E_\mathrm{corr}(R_q, q) - E_\mathrm{corr}(R'_q, q')}{q' - q} - \epsilon_\mathrm{v} \tag{S1}$$

where $E[X^q(R_q)]$ and $E[X^{q'}(R_{q'})]$ are the total energies of the defective systems with charge q and q' at their respective geometries, R_q and $R_{q'}$, and ϵ_v is the valence band maximum (VBM) of the neutral pristine g-C_3N_4 monolayer.

$E_{\mathrm{corr}}[X(R_q, q)]$ and $E_{\mathrm{corr}}[X(R'_q, q')]$ represent electrostatic finite-size corrections accounting for the spurious interactions due to the presence of a charged periodic supercell. This correction is here evaluated for relaxed V_N^- and V_N^+ defects using the `sxdefectalign2d` computational tool,[21] expressly designed to correct the total energy of two-dimensional systems bearing a localized charge. This approach solves the Poisson equation for a Gaussian charge distribution within a position-dependent dielectric medium under both periodic and open boundary conditions and computes the energy difference $\Delta E_{\mathrm{corr}} = E_{\mathrm{isolated}} - E_{\mathrm{periodic}}$ to extrapolate the physically relevant limit of the isolated defect. Corrections up to 0.36 eV for the systems considered in this study. Similarly, when dealing with vertical transitions, such as those that can be probed via optical measurements, we can define a vertical transition level in which the nuclear coordinates of the defect are kept frozen i.e. $E_{\mathrm{f}}[X^q(R_q)] = E_{\mathrm{f}}[X^{q'}(R_q)]$:

$$\begin{aligned}\mu^{\mathrm{opt}}_{q\to q'}(X^q/X^{q'}) = &\frac{E[X^q(R_q)] - E[X^{q'}(R_q)]}{q' - q} \\ &+\frac{E_{\mathrm{corr}}(R_q, q) - E_{\mathrm{corr}}(R_q, q')}{q' - q} - \epsilon_{\mathrm{v}},\end{aligned} \tag{S2}$$

where $\mu^{\mathrm{opt}}_{q\to q'}$ denotes a vertical transition from q to q', while keeping the geometry R_q fixed. $E_{\mathrm{corr}}(R_q, q')$ is the finite-size correction of the supercell upon vertical variation of charge state, defined in Refs. 22,23, and consequently evaluated. Finally, we can define the reorganization energy of the defect upon charge injection/detachment as the absolute difference between the vertical and adiabatic energy levels:

$$\lambda_{q\to q'} = |\mu^{\mathrm{opt}}_{q\to q'}(X^q/X^{q'}) - \mu^{\mathrm{ad}}(X^q/X^{q'})| \tag{S3}$$

S3 Structural and energetic analysis of buckling

Table S2 summarizes the calculated energy difference ($\Delta E_{\mathrm{buckling}}$) between the buckled and planar configurations for pristine g-C_3N_4 and for the three defective structures studied in the main text, using the computational set-up, as presented in Section S1.

Table S2: Energy difference per atom ($\Delta E_{\text{buckling}}$, in eV) between buckled and planar configurations for pristine g-C_3N_4 and for the three defects, using different cell sizes.

Cell type	2×2	4×4	6×6
Pristine	0.027	0.032	0.032
V_N^0(C)	0.034	0.030	0.032
V_N^0(E)	0.022	0.029	0.035
V_N^0(B)	0.045	0.034	0.034

The structural corrugation of the 2D layers is quantified by fitting a best–fit reference plane to the atomic coordinates obtained from the optimized or equilibrated geometries. Given the atomic positions $\{\mathbf{r}_i = (x_i, y_i, z_i)\}$, the plane is defined by its centroid $\mathbf{r}_0$ and normal vector $\mathbf{n}$, obtained by singular value decomposition (SVD) of the centered coordinate matrix. The signed distance of each atom i from the plane, corresponding to its out-of-plane displacement, is then

$$h_i = (\mathbf{r}_i - \mathbf{r}_0) \cdot \mathbf{n}. \tag{S4}$$

From these heights, three statistical descriptors of buckling are defined:

1. The root-mean-square height deviation (RMS_z),

$$\text{RMS}_z = \sqrt{\frac{1}{N} \sum_i h_i^2}, \tag{S5}$$

   which measures the overall roughness of the layer and is sensitive to large local distortions.

2. The mean absolute height (MAH),

$$\text{MAH} = \frac{1}{N} \sum_i |h_i| \tag{S6}$$

3. The largest buckling amplitude (LBA),

$$\text{LBA} = \max_i(h_i) - \min_i(h_i), \tag{S7}$$

corresponding to the maximum buckling height difference within the layer.

A one-dimensional histogram of the height distribution $P(h)$ is then generated to visualize the statistical distribution of atomic displacements (e.g. Figure S3), while a two-dimensional interpolated height map $z(x, y)$ is constructed by cubic interpolation of the $\{x_i, y_i, h_i\}$ triplets over a regular grid. The resulting colormap (e.g. Figure S4) provides a spatial representation of ripples and local deformations across the 2D sheet.

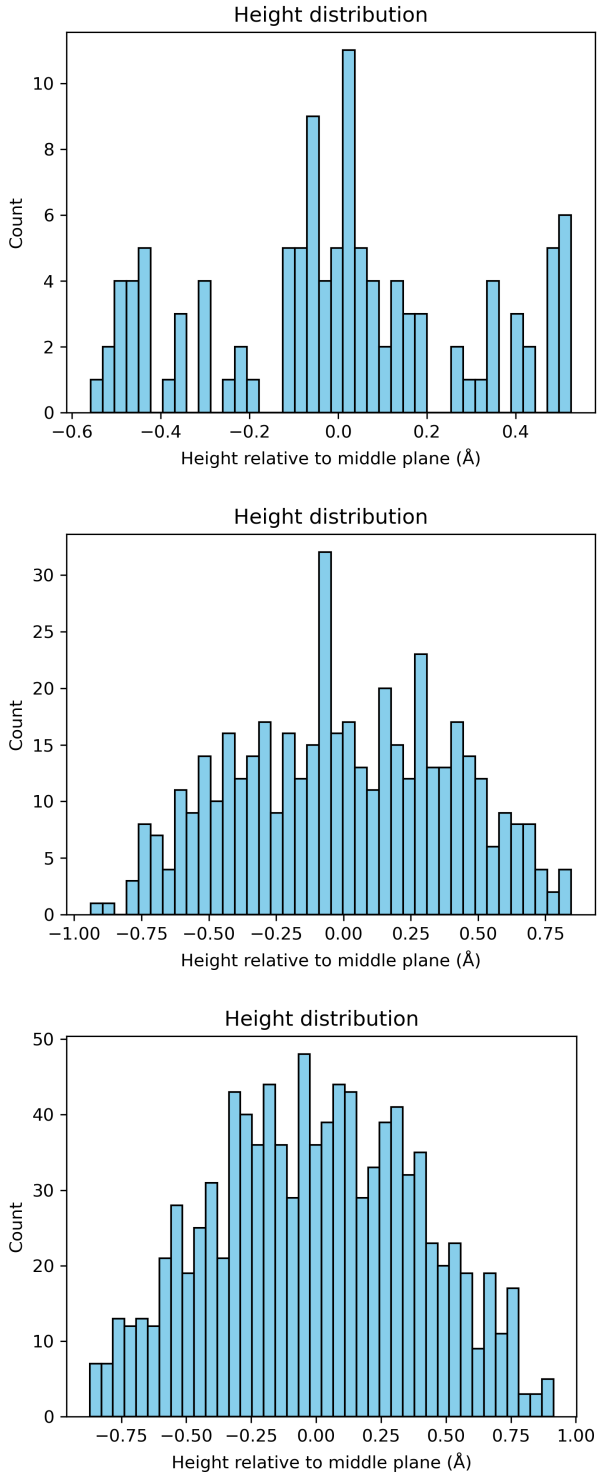

Figure S3: Distribution of atomic heights (z-coordinates relative to the mean plane) in the relaxed g-C_3N_4 structures for 2×2 (top), 4×4 (middle), and 6×6 (bottom) supercells.

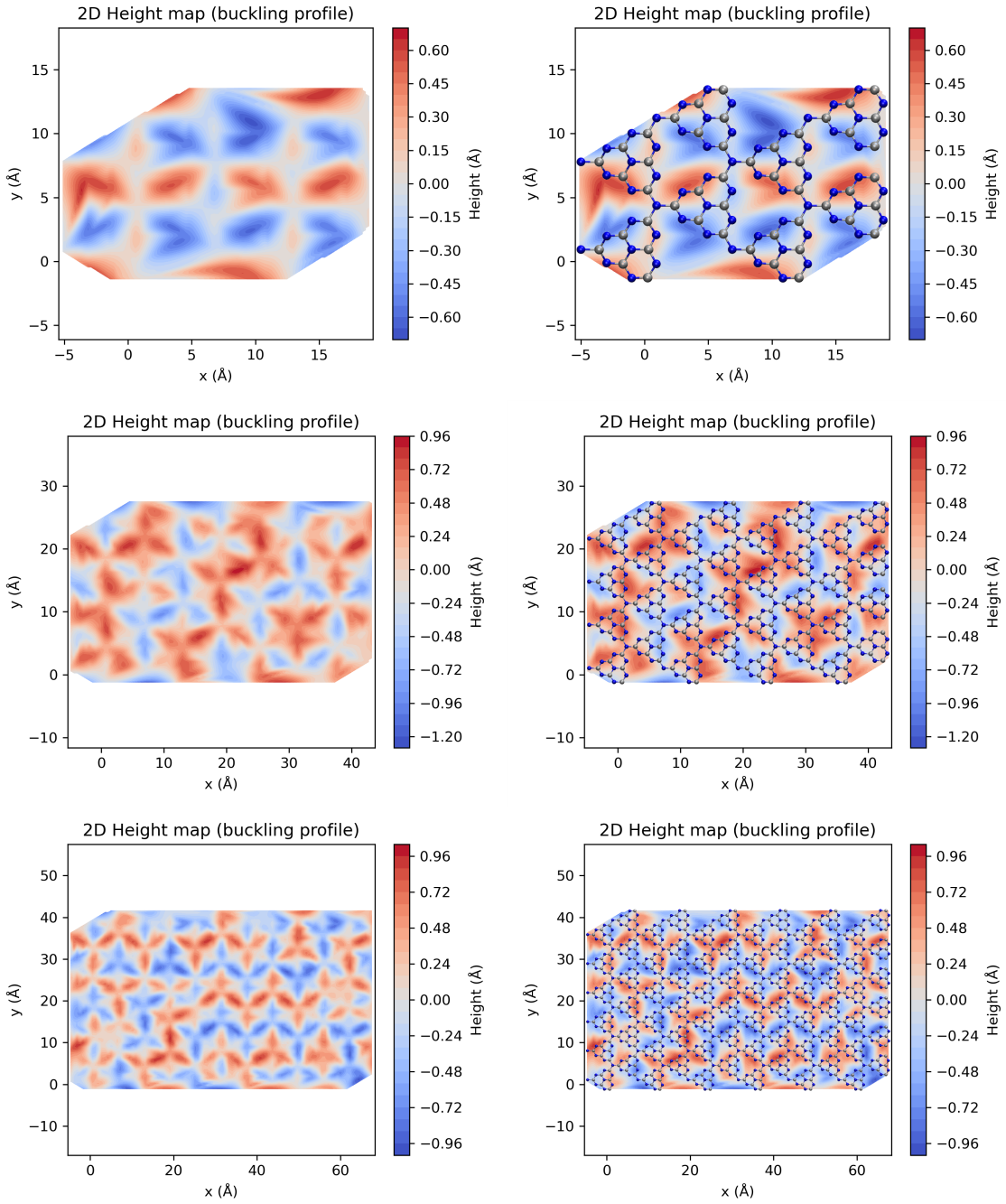

Figure S4: Two-dimensional height maps of the relaxed g-C_3N_4 structures for 2×2 (top), 4×4 (middle), and 6×6 (bottom) supercells. The color scale represents deviations from the mean plane. The emergence of smooth, periodic undulations in the larger cells points toward a delocalized distortion, as expected. On the right, we show the same two-dimensional height maps but with the molecular structure overlayed.

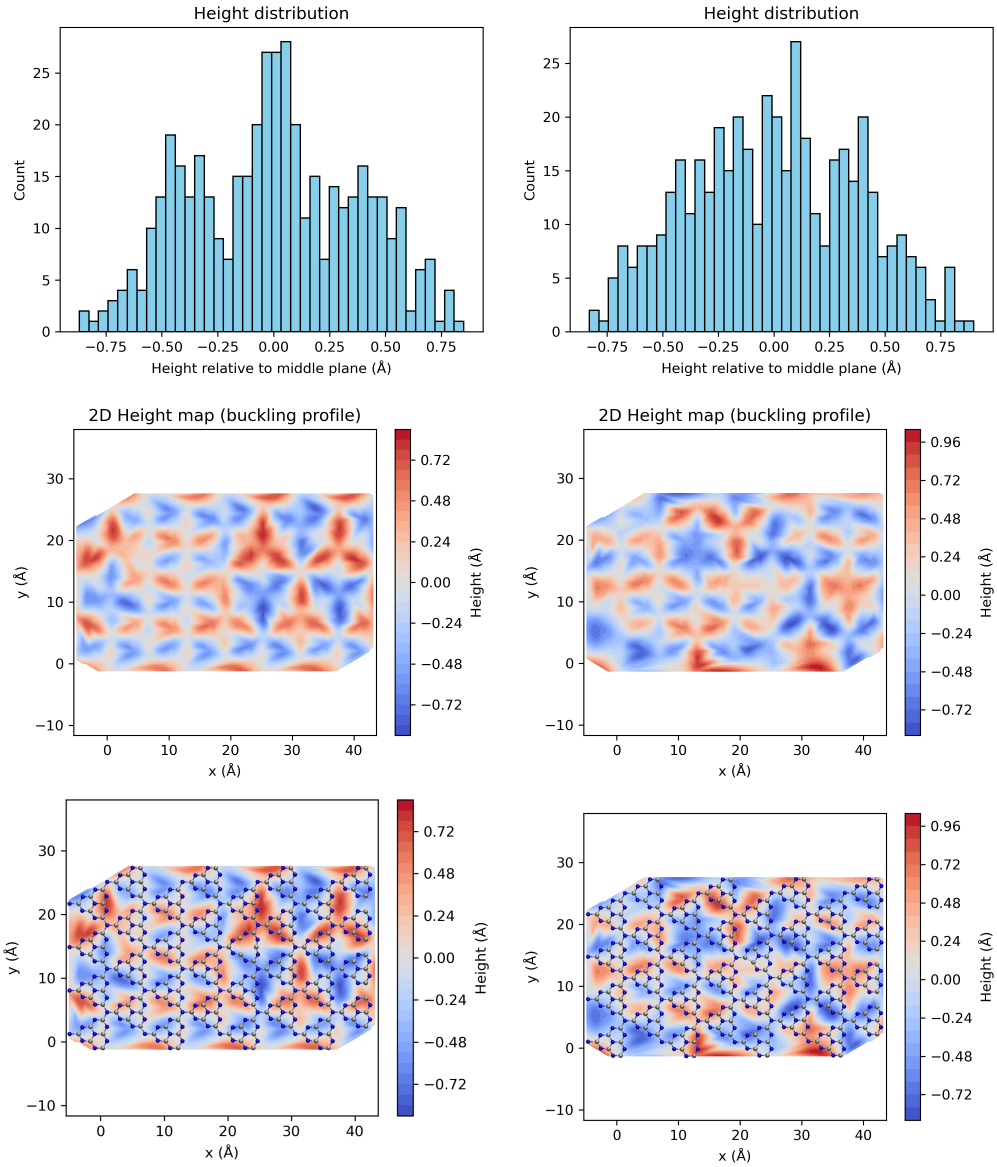

Figure S5: Distribution of atomic heights (z-coordinates relative to the mean plane) (top) and two-dimensional height maps (middle) in the relaxed 4×4 g-C_3N_4 structures for central (left) and edge (right) N vacancy, respectively. In the two bottom panels we show the same two-dimensional height maps but with the molecular structure overlayed.

S4 Total-energy differences between different spin states for neutral and charged defects

Table S3 summarizes the energy differences between doublet and quartet spin states [$\Delta E(D-Q)$] for the neutral defect and between singlet and triplet spin states [$\Delta E(S-T)$] for charged systems, respectively. Different defective g-C_3N_4 structures, at varying supercell size, are reported where available. Inspection of this table shows that the lowest spin state is always the more stable, for all the studied systems.

In Table S4, we report the total-energy differences between the edge and central N vacancies in the differently charged states ($q = \pm 1$), which evidences an interesting inversion in stability between edge and central defect, upon oxidation/reduction.

Table S3: Total energy difference (eV) between doublet and quartet states, $\Delta E(D-Q)$, for V_N^0(C), V_N^0(E), and V_N^0(B) and between singlet and triplet states, $\Delta E(S-T)$, for $V_N^{\pm}$(C) and $V_N^{\pm}$(E). Negative (positive) values indicate that the lowest (highest) spin state is more stable.

Defect	2×2	4×4
V_N^0(C)	-2.51	-3.16
V_N^0(E)	-1.96	-2.65
V_N^0(B)	-1.41	-1.84
V_N^-(C)		-0.67
V_N^-(E)		-0.73
V_N^+(C)		-0.94
V_N^+(E)		-1.08

Table S4: Total energy difference (eV) between V_N^q(E) and V_N^q(C) for $q = +1, -1$, $\Delta E(q)$ in the singlet state for the 4×4 supercell. Negative (positive) values indicate that the edge (central) defect is more stable.

$q = -1$	$q = +1$
-0.59	$+0.35$

S5 Structure and spin density of neutral vacancies for 2×2 and 6×6 supercells

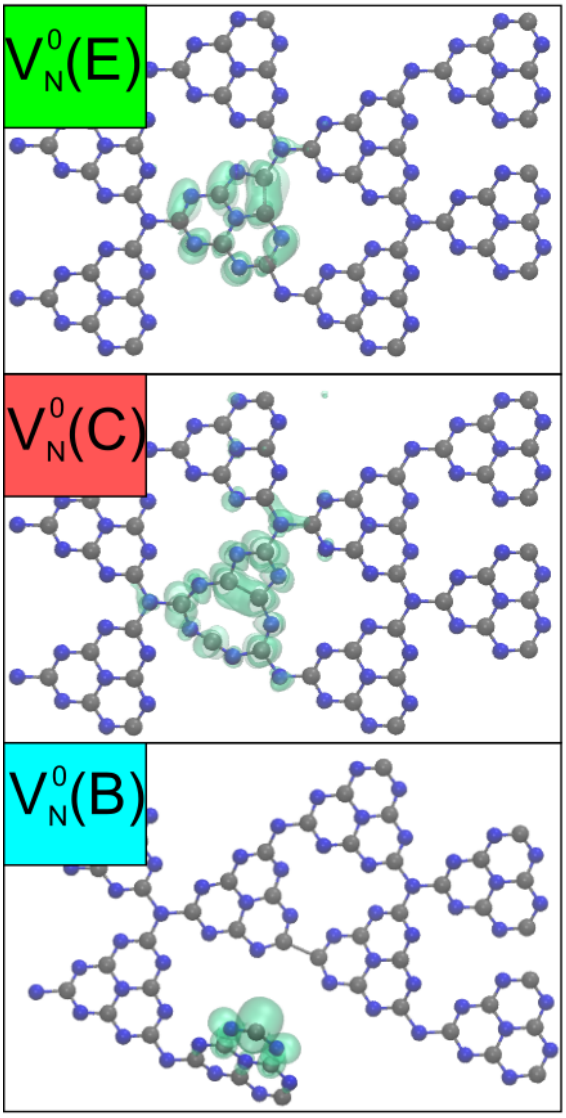

Figure S6: Stick & ball representation of 2×2 optimized structures for monolayer g-C_3N_4 for the different neutral defects. Isodensity representation of the spin density is given in green (isovalue = 0.001 a.u.).

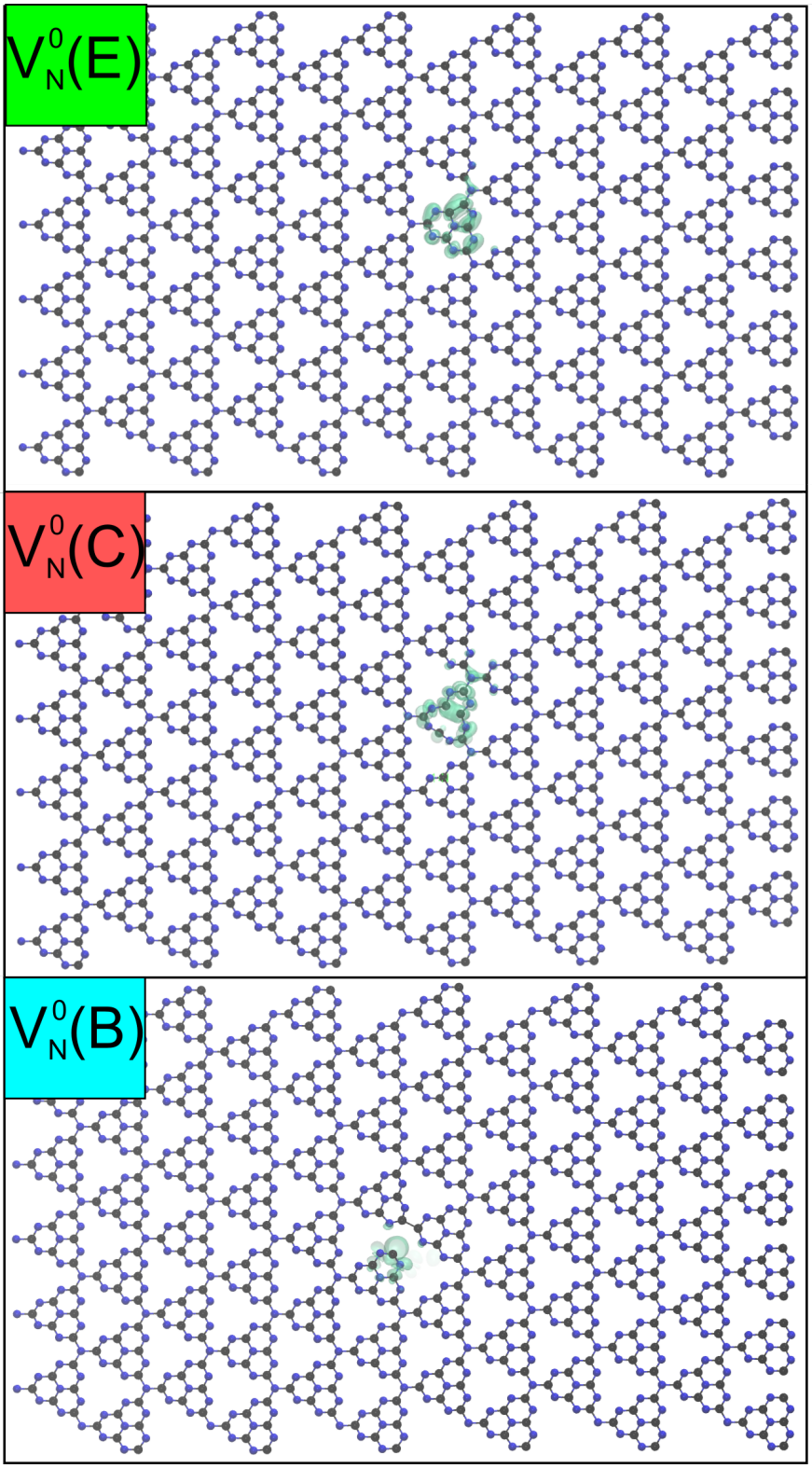

Figure S7: Stick & ball representation of 6×6 optimized structures for monolayer g-C_3N_4 for the different neutral defects. Isodensity representation of the spin density is given in green (isovalue = 0.001 a.u.).

S6 Electronic density of states for bulk and neutral N vacancies

In this section we report the density of states (DOS) for three structures, in Fig. S8

- Pristine g-C_3N_4 (top panel): The DOS shows the expected semiconductor character with a clear band gap. The valence band is dominated by N 2p states (blue), consistent with the nitrogen lone-pair character of the VBM, while both C and N contribute to the conduction band. The gap appears to be approximately 2.7–2.8 eV, consistent with what is reported in the literature (see main text).

- V_N^0(C) (middle panel): A very narrow, spin-polarized in-gap state just below the Fermi level (set to 0 eV), appears. Importantly, the in-gap state appears to sit very close to mid-gap, consistent with the deep donor (+/0) level at 1.70 eV above the VBM reported in Table 2 in the main text.

- V_N^0(E) (bottom panel): Similarly, to the central defect, a sharp spin-polarized in-gap state is visible, again with dominant N character. However, compared to V_N^0(C), the in-gap feature appears slightly closer to the valence band edge, which is qualitatively consistent with the (+/0) donor level of 0.82 eV above the VBM for the edge vacancy (Table 2). The conduction band onset appears similar to the pristine case, with a small peak right before the CBM consistent with the shallow (0/-) acceptor level lying just below the CBM.

Qualitatively, these shallow (0/-) acceptor levels near the CBM are indicative of relatively low electron effective masses and thus favorable electron mobility toward reduction reactions. In contrast, the deep (+/0) donor levels act as hole traps, hindering hole transport to oxidation sites and potentially limiting overall photocatalytic efficiency, in line with the analysis provided in the main text.

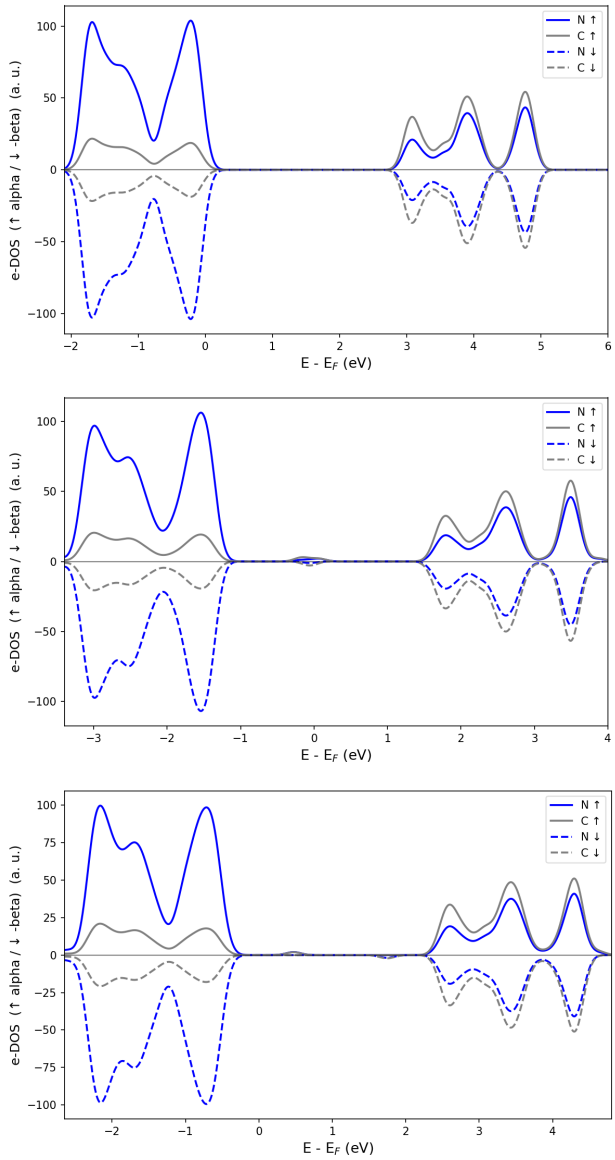

Figure S8: Electronic density of states (e-DOS) (including both spin populations) calculated for pristine g-C_3N_4 (top), V_N^0(C) (middle) and V_N^0(E) (bottom). Color codes: C contribution to the e-DOS in gray, N contribution in blue. Energies are given with respect to the Fermi Energy.

S7 Detailed description of optical energy levels associated with N vacancies

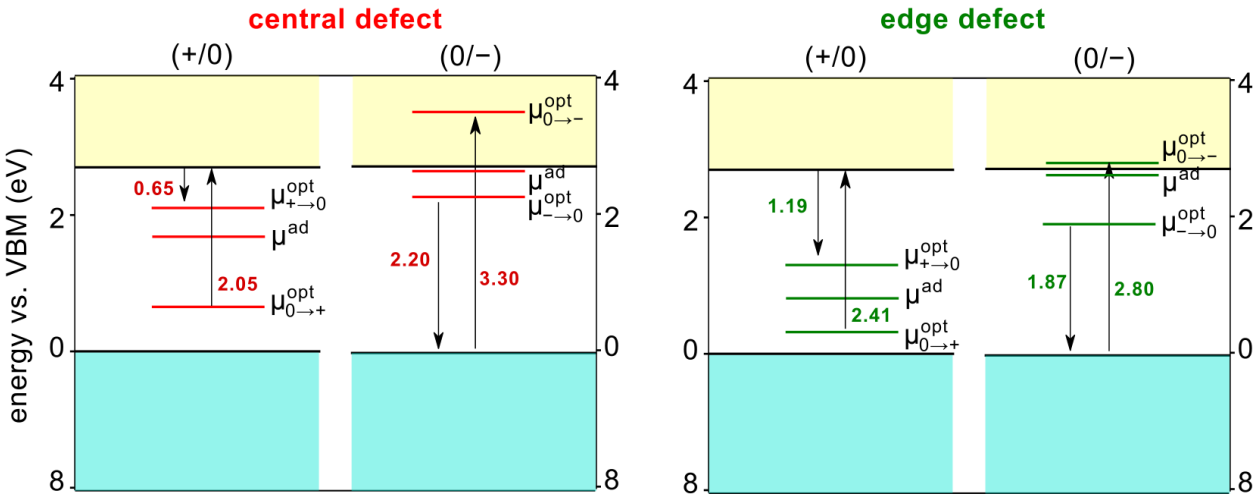

Figure S9: Adiabatic and vertical charge transition levels. The arrows indicates the vertical absorption transitions, together with the transition energy (in eV), without considering the exciton correction (see section S2).

The optical excitation gap associated with defective configurations is evaluated from the vertical charge transition level (CTL) energies reported in Table 2, main text. Since all CTL values are given relative to the valence-band maximum (set to 0 eV), the 0/− levels directly represent the excitation energy for VBM → defect transitions. The defect → CBM excitation energies associated with the 0/+ transition are obtained by subtracting the corresponding CTL energy from the conduction-band minimum energy (2.7 eV for g-C_3N_4, as discussed in main text), see also Figure S9.

For example, from Table 2 in the main text and Figure S9 it is evident that vertical excitation of an electron from the defect to the CBM of the material leads to a transition energy differences of 2.05 and 2.41 eV for the central and edge vacancies. However, as discussed in main text, when accounting for excitonic effects via time-dependent DFT calculations (see section S2 for details) on the neutral defect, these energy gaps are reduced by 0.32 eV, thus leading to the values of 1.73 eV for the central defect and 2.09 eV for the edge defect, as

discussed in the main text.

S8 Reorganization energy of charge carriers in pristine g-C_3N_4

In this Section, we calculate the reorganization energy of charge carriers in pristine g-C_3N_4. We first address the non-interacting hole and electron pair: to this end, we separately injected a hole and an electron in pristine g-C_3N_4 and relax the structures. We defined the hole/electron reorganization energy $\lambda_\pm$ as the energy difference between the charged system ($\pm$) in its relaxed geometry ($R_\pm$) and in the initial neutral ground-state geometryR_0:

$$\lambda_\pm = E(\pm, R_0) - E(\pm, R_\pm) \tag{S8}$$

We calculate exiguous values of 0.07 and 0.08 eV for the hole and the electron respectively (see Table S5), clearly indicating small separation of the potential energy surfaces, resulting from larger delocalization of charge carriers, see Figure S10. Further, we simulate the interacting hole-electron pair considering the lowest-lying triplet exciton and, similarly, we estimate the reorganization energy as the energy difference between the triplet in its optimized geometry and in the initial singlet ground state:

$$\lambda_{T_1} = E(T_1, R_{S_0}) - E(T_1, R_{T_1}) \tag{S9}$$

Table S5: Calculated values (eV) of λ_+, λ_-, and λ_{T_1}, as defined in Equations S8 and S9.

λ_i	Value
λ_+	0.07
λ_-	0.08
λ_{T_1}	0.10

In this case, we calculate a reorganization energy of 0.1 eV, again consistent with a semi-localized charge state, cf. Figure S10, even if excitonic interaction between charge carriers produce a somewhat more pronounced localization. All these calculated values point to small

differences between the vertical and adiabatic band gap of pristine g-C_3N_4 and ensure that reduced PL observed for N-poor samples is not related with band-to-band transitions

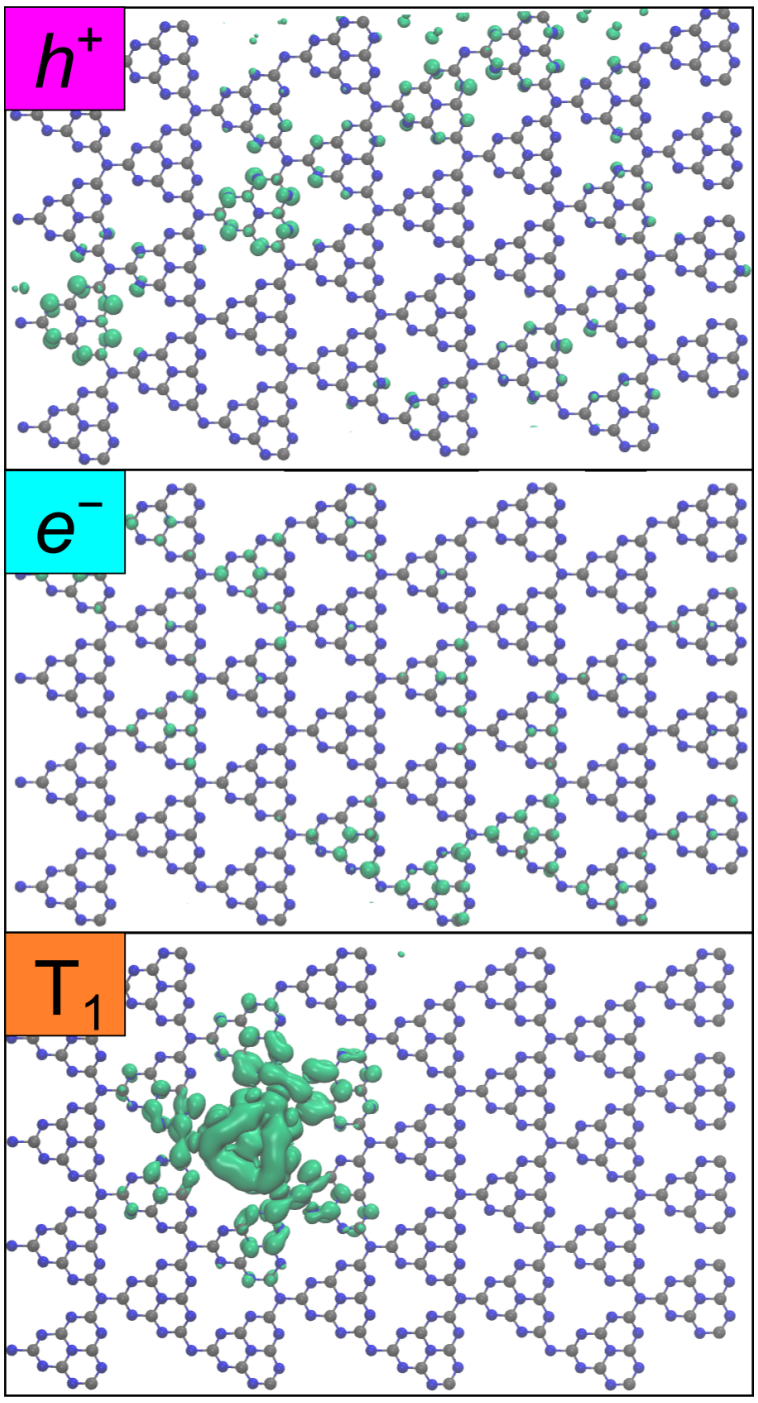

Figure S10: Stick & ball representation of 4×4 optimized structures for monolayer g-C_3N_4 bearing an extra hole (top), an extra electron (middle), the lowest triplet exciton (bottom). Isodensity representation of the spin density is given in green (isovalue = 0.001 a.u.).

References

(1) VandeVondele, J.; Krack, M.; Mohamed, F.; Parrinello, M.; Chassaing, T.; Hutter, J. Quickstep: Fast and Accurate Density Functional Calculations Using a Mixed Gaussian and Plane Waves Approach. *Comput. Phys. Commun.* **2005**, *167*, 103 – 128.

(2) VandeVondele, J.; Hutter, J. Gaussian Basis Sets for Accurate Calculations on Molecular Systems in Gas and Condensed Phases. *J. Chem. Phys.* **2007**, *127*, 114105.

(3) Kühne, T. D. et al. CP2K: An electronic structure and molecular dynamics software package - Quickstep: Efficient and accurate electronic structure calculations. *J. Chem. Phys.* **2020**, *152*, 194103.

(4) Hartwigsen, C.; Goedecker, S.; Hutter, J. Relativistic Separable Dual-Space Gaussian Pseudopotentials from H to Rn. *Phys. Rev. B* **1998**, *58*, 3641–3662.

(5) Guidon, M.; Schiffmann, F.; Hutter, J.; VandeVondele, J. Ab Initio Molecular Dynamics Using Hybrid Density Functionals. *J. Chem. Phys.* **2008**, *128*, 214104.

(6) Guidon, M.; Hutter, J.; VandeVondele, J. Robust Periodic Hartree-Fock Exchange for Large-Scale Simulations Using Gaussian Basis Sets. *J. Chem. Theory Comput.* **2009**, *5*, 3010–3021.

(7) Guidon, M.; Hutter, J.; VandeVondele, J. Auxiliary Density Matrix Methods for Hartree-Fock Exchange Calculations. *J. Chem. Theory Comput.* **2010**, *6*, 2348–2364.

(8) Ambrosio, F.; Landi, A.; Loriso, M.; Leo, A.; Peluso, A. External Reorganization Energy upon Charge Transfer Reactions in Mildly Polar Media: The Case of Naphthalene in Tetrahydrofuran. *J. Phys. Chem. Lett.* **2025**, *16*, 6734–6744.

(9) Perdew, J. P.; Zunger, A. Self-Interaction Correction to Density-Functional Approximations for Many-Electron Systems. *Phys. Rev. B* **1981**, *23*, 5048–5079.

(10) Zhang, Y.; Yang, W. A Challenge for Density Functionals: Self-Interaction Error Increases for Systems with a Noninteger Number of Electrons. *J. Chem. Phys.* **1998**, *109*, 2604–2608.

(11) Romani, L.; Speltini, A.; Dibenedetto, C. N.; Listorti, A.; Ambrosio, F.; Mosconi, E.; Simbula, A.; Saba, M.; Profumo, A.; Quadrelli, P.; De Angelis, F.; Malavasi, L. Experimental Strategy and Mechanistic View to Boost the Photocatalytic Activity of Cs3Bi2Br9 Lead-Free Perovskite Derivative by g-C3N4 Composite Engineering. *Adv. Funct. Mater.* **2021**, *31*, 2104428.

(12) Vydrov, O. A.; Van Voorhis, T. Nonlocal van der Waals Density Functional: The Simpler the Better. *J. Chem. Phys.* **2010**, *133*, 244103.

(13) Sabatini, R.; Gorni, T.; de Gironcoli, S. Nonlocal van der Waals Density Functional Made Simple and Efficient. *Phys. Rev. B* **2013**, *87*, 041108.

(14) Chen, W.; Griffin, S. M.; Rignanese, G.-M.; Hautier, G. Nonunique fraction of Fock exchange for defects in two-dimensional materials. *Phys. Rev. B* **2022**, *106*, L161107.

(15) Alkauskas, A.; Broqvist, P.; Pasquarello, A. Defect Energy Levels in Density Functional Calculations: Alignment and Band Gap Problem. *Phys. Rev. Lett.* **2008**, *101*, 046405.

(16) Alkauskas, A.; Broqvist, P.; Pasquarello, A. Defect Levels through Hybrid Density Functionals: Insights and Applications. *Phys. Status Solidi B* **2011**, *248*, 775–789.

(17) Ambrosio, F.; Miceli, G.; Pasquarello, A. Redox Levels in Aqueous Solution: Effect of van der Waals Interactions and Hybrid Functionals. *J. Chem. Phys.* **2015**, *143*, 244508.

(18) Freysoldt, C.; Neugebauer, J.; Van de Walle, C. G. Fully *Ab Initio* Finite-Size Corrections for Charged-Defect Supercell Calculations. *Phys. Rev. Lett.* **2009**, *102*, 016402.

(19) Komsa, H.-P.; Rantala, T. T.; Pasquarello, A. Finite-Size Supercell Correction Schemes for Charged Defect Calculations. *Phys. Rev. B* **2012**, *86*, 045112.

(20) Loriso, M.; Azmat, S.; Listorti, A.; Landi, A.; Wiktor, J.; De Angelis, F.; Peluso, A.; Colella, S.; Ambrosio, F. Electron localization and mobility in layered Cs3Bi2Br9 perovskite: consequences on photocatalytic processes. *J. Phys. Energy* **2025**, *8*, 015009.

(21) Freysoldt, C.; Neugebauer, J. First-principles calculations for charged defects at surfaces, interfaces, and two-dimensional materials in the presence of electric fields. *Phys. Rev. B* **2018**, *97*.

(22) Falletta, S.; Wiktor, J.; Pasquarello, A. Finite-size corrections of defect energy levels involving ionic polarization. *Phys. Rev. B* **2020**, *102*, 041115.

(23) Ambrosio, F.; Chen, W.; Pasquarello, A. Electronic energy levels of aqueous hydroxyl species. *Phys. Chem. Chem. Phys.* **2025**, *27*, 23079–23090.